PCCP

Accepted Manuscript

ROYAL SOCIETY OF CHEMISTRY

www.rsc.org/pccp

PCCP

PAPER

Geometric and electronic structures of the synthetic Mn_4CaO_4 model compound mimicking the photosynthetic oxygen-evolving complex

Received 00th January 20xx,
Accepted 00th January 20xx

DOI: 10.1039/x0xx00000x

www.rsc.org/

Mitsuo Shoji,*[ab] Hiroshi Isobe,[c] Jian-Ren Shen[c] and Kizashi Yamaguchi[de]

Water oxidation by photosystem II (PSII) converts light energy into chemical energy with the concomitant production of molecular oxygen, both of which are indispensible for sustaining life on the Earth. This reaction is catalyzed by an oxygen-evolving complex (OEC) embedded in the huge PSII complex, and its mechanism remains elusive in spite of extensive studies of the geometric and electronic structures. In order to elucidate the water-splitting mechanism, synthetic approaches have been extensively employed to mimic the native OEC. Very recently, a synthetic complex $[Mn_4CaO_4(Bu^tCOO)_8(py)(Bu^tCOOH)_2]$ (**1**) closely mimicking the structure of the native OEC was obtained. In this study, we extensively examined the geometric, electronic and spin structures of **1** using the density functional theory method. Our results showed that the geometric structure of **1** can be accurately reproduced by theoretical calculations, and revealed many similarities in the ground valence and spin states between **1** and the native OEC. We also revealed two different valence states in the one-electron oxidized state of **1** (corresponding to the S_2 state), which lie in the lower and higher ground spin states (S = 1/2 and S = 5/2), respectively. One remarkable difference between **1** and the native OEC is the presence of a non-negligible antiferromagnetic interaction between the Mn1 and Mn4 sites, which slightly influenced their ground spin structures (spin alignments). The major reason causing the difference can be attributed to the short Mn1–O5 and Mn1-Mn4 distances in **1**. Introduction of the missing O4 atom and the reorientation of the Ca coordinating ligands improved the Mn1-O5 and Mn1-Mn4 distances comparable to the native OEC. These modifications will therefore be important for the synthesis of further advanced model complexes more closely mimicking the native OEC beyond **1**.

1. Introduction

Photosynthesis converts light energy into chemical potentials through a series of light-induced proton-coupled electron transfer reactions. During oxygenic photosynthesis, the water molecule is used as the ultimate reductant by photosystem II (PSII) to generate molecular dioxygen via the water-splitting reaction:

$$2H_2O + 4h\nu \rightarrow O_2 + 4e^- + 4H^+ . \qquad (1)$$

This reaction, first invented by cyanobacteria ~2.7 billion years ago, transformed the atmosphere from anaerobic to an aerobic one, thereby supporting all aerobic life on the Earth.[1] The reaction is catalyzed by an oxygen evolving complex (OEC) embedded in the protein matrix of PSII, which consists of one calcium and four manganese atoms linked by five oxo (or hydroxo) bridges and is designated as the Mn_4CaO_5 cluster.[2,3] Elucidation of the catalytic process for water splitting in OEC is important not only for fundamental biology, but also for the design of efficient artificial catalysts for water oxidation made by abundant 3d transition metals such as Mn, Fe, Co, etc.

Substantial efforts have been made to elucidate the reaction mechanism including the water splitting and O-O bond formation reactions in the OEC.[4-7] The structure of PSII has been analyzed up to a resolution of 1.9 Å by X-ray diffraction (XRD) using intense synchrotron radiation X-rays,[2] although the structure obtained may contain experimental uncertainties as well as some X-ray radiation damage.[8] Very recently, the radiation-damage-free structure of PSII has been analyzed at a resolution of 1.95 Å using a femtosecond X-ray free electron laser (XFEL), providing a more reliable S_1-state structure.[3] The radiation damage-free structure showed shorter Mn-Mn distances than those previously obtained using the synchrotron radiation X-rays; however, there are still small differences among the Mn-Mn and Mn-O distances between the results of the XRD and extended X-ray absorption fine spectroscopic (EXAFS) analyses.[9] Moreover, no detailed structures for the higher oxidation states (S_2 and S_3) have been experimentally determined. Although the structure of the S_3 state was recently reported using the similar XFEL methodology,[10,11] the obtained results were at a low resolution, and conflicting results were reported by two

---

[a] *Center for Computational Sciences, University of Tsukuba, Tennodai 1-1-1, Tsukuba 305-8577, Japan*
[b] *Graduate School of Pure and Applied Sciences, University of Tsukuba, Tennodai 1-1-1, Tsukuba 305-8571, Japan. E-mail: mshoji@ccs.tsukuba.ac.jp*
[c] *Photosynthesis Research Center, Graduate School of Natural Science and Technology, Okayama University, Okayama 700-8530, Japan*
[d] *Institute for NanoScience Design, Osaka University, Toyonaka, Osaka 560-0043, Japan*
[e] *Handairigaku Techno-Research (NPO), Toyonaka, Osaka 560-0043, Japan*

† Electronic Supplementary Information (ESI) available: [details of any supplementary information available should be included here]. See DOI: 10.1039/x0xx00000x

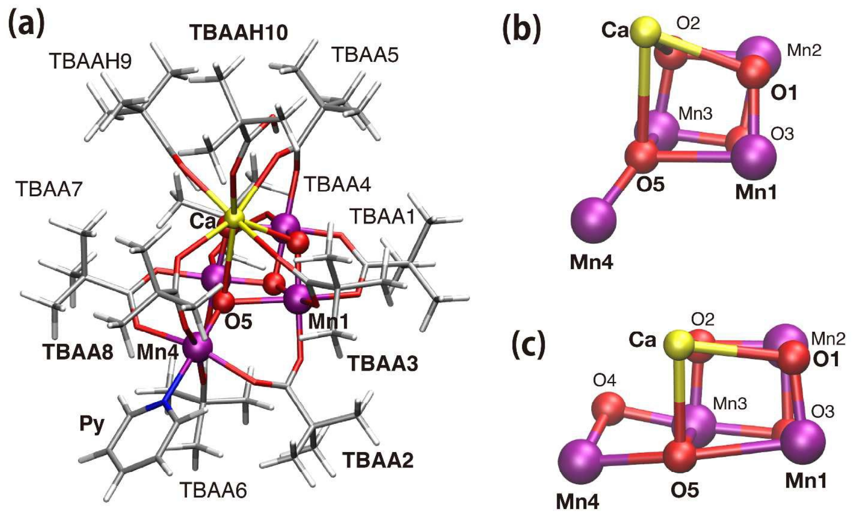

Fig. 1 (**a**) Molecular structure of the synthetic model [$Mn_4CaO_4(Bu^tCOO)_8(py)(Bu^tCOOH)_2$] (**1**) optimized using the broken symmetry density functional theory level at the neutral (S_1) state (*Sz*=1/2). The Bu^tCOO ligand is abbreviated as TBAA. (**b**) Enlarged view of the Mn_4CaO_4 core structure of **1**. (**c**) Corresponding Mn_4CaO_5 core structure of the native OEC (PDBID: 4UB6). Color: Ca, yellow; Mn, purple, H, white; C, gray; N, blue.

groups. Therefore, revealing the OEC reaction mechanism remains a challenging issue mostly due to the ultrafine geometries with sensitive electronic and spin properties of the Mn_4CaO_5 cluster that is buried in the huge protein complex PSII.

In order to better reveal the properties and reaction mechanism of the Mn_4CaO_5 core, synthetic approaches to obtain model complexes mimicking the native Mn_4CaO_5 cluster have been extensively explored.[12-15] The asymmetric Mn_3Ca cubane core of the OEC was indeed obtained in some synthetic complexes. For example, Kandy et al. synthesized a model complex containing the [$Mn(IV)_3CaO_4$] core[12], and Mukherjee et al. obtained a complex containing the [$CaMn(IV)_3CaO_4$] core in which one Ca ion is attached to the [Mn_3CaO_4] cubane[13]. However, the Mn valence states of these complexes are all Mn(IV), which differ from the $Mn(III)_2Mn(IV)_2$ oxidation state proposed for the dark stable S_1 state of the native OEC.

Very recently, Zhang et al. succeeded in synthesizing the model complex, $Mn_4CaO_4(Bu^tCOO)_8(py)(Bu^tCOOH)_2$ (Bu^t, tert-butyl; py, pyridine), hereafter labeled **1**, which well reproduced some of the structural and functional features of the native OEC.[15] The complex **1** contains a [Mn_4CaO_4] core in which a dangling Mn ion is attached to a [Mn_3CaO_4] cubane as that proposed in the London structure of the OEC (Figure 1).[16] The Mn valence state of **1** is $Mn(III)_2Mn(IV)_2$, and it was shown that **1** can undergo a sequential one-electron oxidation. After the first one-electron oxidation, two characteristic electronic paramagnetic resonance (EPR) signals, a multiline signal and a $g > 4.0$ signal, were observed, which are very similar to those observed with the native OEC[15]. Therefore, **1** is expected to resemble the native OEC not only regarding the geometric structure, but also the electronic structure, and represents an excellent synthetic model for the native OEC in the S_1 and S_2 states. Investigations of the characteristic features of **1** may provide important clues for further understanding the inherent nature of the Mn_4CaO_X (X = 4,5) cluster.

In the present study, the structural, electronic and spin properties of **1** were investigated for comparison with the results of the native OEC at the same broken-symmetry (BS) density functional theory level. The Mn valence and spin states were determined for the four oxidation states (S_0 - S_3), and their magnetic and ground spin states are analyzed by evaluating all the effective exchange interactions for the Heisenberg spin Hamiltonian. In order to reveal the reason why the Mn1-Mn4 length is shorter in **1**, we modeled the complex by substituting the carboxyl ligands with water molecules and introducing the missing oxo atom (O4); the results showed how the Mn1-Mn4 and Mn1-O5 lengths are elongated to the values of the native OEC. Our results provide important information for the further synthesis of model complexes more closely resembling the native OEC.

2. Computational details

2.1 Quantum mechanical calculations

The full structural model of **1** was used for the geometric and electronic structure calculations. For the theoretical modeling study, a reduced model, [$Mn_4CaO_4(AcO)_8(py)(AcOH)_2$], referred to as **2** was used, in which all the original carboxyl ligands, i.e., pivalic acids (Bu^tCOO: TBAA), were modeled as acetic acids (AcO) to reduce the computational costs. The initial coordinates for both models were taken from the X-ray structure of **1**[15]. By adding all the hydrogen atoms, the total molecular charge became zero in the $Mn(III)_2Mn(IV)_2$ valence state (S_1 state). Atoms in the Mn_4CaO_4 cluster were labeled in the same manner as those in the native OEC, i.e., one Ca, four Mn (Mn1-Mn4) and four O atoms (O1-O5 except for O4) were assigned in the Mn_4CaO_4 core (see Figure 1). The carboxyl ligands were sequentially indexed from TBAA1 (AcO1) to TBAAH10 (AcOH10) as illustrated in Figure 1. TBAAH9(AcOH9) and TBAAH10(AcOH10) are ligands coordinated to Ca and are considered to be protonated due to mono-coordination to the Mn_4CaO_4 core. As **1** is only stable in hydrophobic organic solvents, all the calculations were performed in a vacuum.

The broken-symmetry (BS) approach has now been established as a practical tool especially for transition metal complexes and metalloproteins (see supporting material S1).[17-22] By the proper selection of the DFT functionals, the geometric structures and magnetic properties can be well reproduced at the BS level. Following past reports,[23-25] UB3LYP/DZVP was employed for the full geometric optimizations and magnetic interaction calculations. The DZVP basis set represents LANL-2DZ for Mn and Ca and 6-31G* for the other atoms. We also performed UBLYP/DZVP level calculations, which yield characteristically similar results and are summarized in the supporting material. The NWChem 6.1 program package was used for all of the QM calculations[26].

The full geometric optimizations for **1** were carried out under iterative procedures for determining the most stable spin configuration. The procedure is explained as follows. In the first step, a full geometric optimization was performed at the highest spin (HS) configuration, then all of the spin configurations were calculated at the broken-symmetry level at the HS optimized structure. We utilized the localized natural orbitals to enhance the fast SCF convergences for the broken-symmetry calculations[27]. If the most stable configuration is found not to be the HS configuration used in the first step, a further geometric optimization was performed in the most stable spin configuration in the next step, and subsequently, all the spin configurations were calculated to check the validity of the most stable spin state. If another spin configuration is found to be more stable than the calculated spin configuration, additional optimizations are iteratively performed in the most stable spin configuration. In this study, three-step optimizations at most were required.

The ground and lower-lying spin states of the model complex were determined by the EPR spectroscopy that used the spin Hamiltonian model for analysis of the observed spectra[15]. In order to determine the spin states for the ground and low-lying excitation states of **1**, the total energies of the eight BS spin configurations were mapped into effective exchange integrals (J) among the Mn spin sites in the Heisenberg spin Hamiltonian. The orbital averaged inter-site J_{ab} values were defined by the $H = -2\Sigma J_{ab}S_aS_b$ where S_a denotes a local spin at site a (a=1-4). Six effective exchange integrals (J_{ab}) were calculated by the least square fitting of the eight broken-symmetry solutions using the generalized spin projection methodology[28] assuming the optimized geometry of the ground spin configuration in each valence state. The exact diagonalization of the *ab initio* spin Hamiltonian model consisting of the calculated J values provided the energy levels of the ground and excited states, and the spin projection factors that are crucial for the theoretical investigation of the EPR spectra and optical spectra.

3. Results and discussion

3.1 Optimized structures

Full geometry optimizations for **1** were performed at the UB3LYP/DZVP level in the four oxidation states (S_0, S_1, S_2 and S_3 states). Two different valence states were obtained with very close energy levels in the S_0 and S_2 states. From the atomic spin density distributions for the Mn sites, the calculated lowest S_0 states were assigned as:

S_0(a):(Mn1(III), Mn2(IV), Mn3(III), Mn4(III))
with (s_{z1}=4/2, s_{z2}=–3/2, s_{z3}=4/2, s_{z4}=–4/2),
S_0(b):(Mn1(III), Mn2(IV), Mn3(IV), Mn4(II))
with (s_{z1}=–4/2, s_{z2}=3/2, s_{z3}=–3/2, s_{z4}=5/2).

The notations in parentheses (a and b) are unique identification characters roughly taken from the Mnx site index (x) in the higher valence state (x=1, 2, 3, 4 correspond to d, c, b, a, respectively). The calculated Mnx-O5 distances are R(Mn4(III)-O5)=1.74Å and R(Mn3(III)-O5)=2.19Å in the S_0(a) state for the lowest spin configuration ((↑ ↓ ↑ ↓) BS structure), and become R(Mn4(II)-O5)=2.05Å and R(Mn3(IV)-O5)=1.76Å in the S_0(b) state optimized at the lowest spin configuration ((↓ ↑ ↓ ↑) BS structure). This is consistent with the fact that the higher oxidation state of Mn will shorten the Mn-O distances. The S_0(a) and S_0(b) states can be converted by an internal electron transfer between Mn4 and Mn3, and only the bond distances around the Mn4 and Mn3 are different. Around Mn4, the bond lengths of R(Mn4-O5), R(Mn4-N:Py), R(Mn4-O:TBAA6) and R(Mn4-O: TBAA8) are elongated in S_0(b) by ~0.1 Å compared to S_0(a). On the other hand, for Mn3, the bond lengths of R(Mn3-O5) and R(Mn3-O:TBAA4) are shortened from the S_0(a) to S_0(b) transition by 0.43 Å and 0.15 Å, respectively. Therefore, the position of O5 was slightly shifted by the change in the oxidation states of Mn4 and Mn3 between the two different S_0 valence states.

From the viewpoint of the structural symmetry breaking (SSB) of the Mn_4CaO_5 structure,[29] the O5 position can be well characterized using the following value:

$$\delta R\text{O5} = [R(\text{Mn1-O5}) - R(\text{Mn4-O5})]/2. \qquad (2)$$

The characteristic δRO5 value by XRD and XFEL were δRO5 = 0.55~0.60 Å for the Mn_4CaO_5 cluster of the native OEC in the S_1 state.[29] On the other hand, the calculated δRO5 values of **1** are 0.23, 0.12 and 0.22 Å for S_0(a), S_0(b) and the X-ray structure, respectively. These values indicate that the calculated S_0(a) state and X-ray structure of **1** can be classified as the right opened structure (R), although the magnitude of these SSB parameters were reduced to about one half as compared to that of the native OEC[26]. On the other hand, S_0(b) is regarded as a central (C) structure.

The relative energy of S_0(a) is slightly more stable than that of S_0(b) by ΔE= 2.86 kcal mol^{-1} between the lowest BS configurations. The energy difference is corrected to ΔE = 2.85 kcal mol^{-1} after the spin projection based on the spin Hamiltonian[28]. More details are discussed in Section 3.3.

The structure of one more reduced state (S_{-1}) in the highest spin configuration was also optimized, which showed that the Mn valence states are S_{-1}:(Mn1(III), Mn2(IV), Mn3(III), Mn4(II)). In this state, the proton is transferred from TBAAH9 to the O2

Table 1. RMSD (Å) between **1** in the different oxidation states and the X-ray structures. All of the states were fully optimized at the UB3LYP/DZVP level.

Valence	S_{-1}	S_0(a)	S_0(b)	S_1	S_2(R)	S_2(C)	S_3
Spin	↑↑↑↑	↑↓↑↓	↓↑↓↑	↑↓↑↓	↑↓↑↓	↑↑↑↓	↑↑↑↓
Non-H	0.583	0.521	0.514	0.447	0.614	0.652	0.611
Mn_4CaO_4	0.117	0.096	0.061	0.063	0.158	0.147	0.189
Mn_4Ca	0.111	0.084	0.051	0.070	0.172	0.161	0.211

of Mn_4CaO_4, and the Mn3-O2 bond is elongated up to *R*(Mn3-O2)=2.23 Å from *R*(Mn3-O2)=1.87 Å in S_0(a). Therefore, the Mn_4CaO_4 cluster is broken in this reduced state (S_{-1}).

The valence state of **1** in the S_1 state was calculated to be (Mn1(III), Mn2(IV), Mn3(IV), Mn4(III)), and no other stable valence states were obtained. The bond-valence sum (BVS) analysis[30-32] also predicted the same valence state using the optimized structure (see the supporting material (Table S2.1)). The valence state is the same as that deduced from the bond valence sum (BVS) analysis of the crystal structure, as well as that of the native OEC[3]. The lowest BS spin configuration is (s_{z1}=4/2, s_{z2}=–3/2, s_{z3}=3/2, s_{z4}=–4/2), though the (s_{z1}=–4/2, s_{z2}=3/2, s_{z3}=3/2, s_{z4}=4/2) BS configuration is also similarly stable. The δ*R*O5 value for the S_1 state is 0.29 Å, consistent with that of the experimentally determined S_1 state structure, indicating that the S_1 state of **1** can be classified as the R structure.

Two different valence states were calculated by the one-electron oxidation of the S_1 state, which corresponds to the S_2 state. Their δ*R*O5 values were 0.32 and -0.14 Å, respectively. These structures can be categorized as R and central (C) structures, respectively, since the latter low δ*R*O5 value indicates an almost symmetrical Mn1-O5-Mn4 bond. Based on the atomic spin density distributions, their electronic structures can be assigned as:

S_2(R): (Mn1(III), Mn2(IV), Mn3(IV), Mn4(IV))
 with (s_{z1}=4/2, s_{z2}=–3/2, s_{z3}=3/2, s_{z4}=–3/2),
S_2(C): (Mn1(IV), Mn2(IV), Mn3(IV), Mn4(III))
 with (s_{z1}=3/2, s_{z2}=3/2, s_{z3}=3/2, s_{z4}=–4/2).

These valence states were in accord with the BVS analysis (Table S2.1) and are consistent with the same valence states of the native OEC in the S_2 state[33, 34]. The S_2(C) state was slightly more stable than S_2(R) by 0.67 kcal mol^{-1} after the spin projection correction. In the native OEC, the S_2(R) state was more stable than S_2(L) by 2~12 kcal mol^{-1}, depending on the QM and QM/MM computational models used for PSII[35,36]. Compared to the native OEC, the shift of O5 by the internal electron transfer from Mn4 to Mn1 is found to very easily occur; this can be attributed to the geometric feature of the short Mn1-Mn4 and Mn*x*-O5 (x=1, 3, 4) distances in **1**.

Upon the one-electron oxidation from the S_2(C) state, no characteristic structural deformations were observed in the S_3 state. The formal valence state revealed by the spin density distribution and BVS analyses was found to be (Mn1(IV), Mn2(IV), Mn3(IV), Mn4(IV)), and the δRO5 value was 0.08 Å, indicating that the S_3 state is essentially regarded as a central structure (S_3(C)), because Mn(IV) does not induce any Jahn-Teller distortions. Thus the DFT calculations revealed the geometrical and valence structure of **1** in the S_i (*i* = –1 - 3) states as summarized in Figure 2.

The RMSDs for all of the heavy-atoms relative to the experimentally determined structure of complex **1** were 0.583 Å, 0.521 Å, 0.514 Å, 0.447 Å, 0.614 Å, 0.652 Å and 0.611 Å for the S_{-1}, S_0(a), S_0(b), S_1, S_2(R), S_2(C) and S_3 state structures, respectively (Table 1). As the RMSD value is the lowest in the S_1 state, the X-ray structure represents the S_1 state structure. For the reduced model **2**, where the t-butyl groups were replaced with acetyl group, the corresponding heavy-atom RMSDs were 0.785 Å, 0.681 Å, 0.699 Å, 0.438 Å, 0.416 Å, 0.478 Å and 0.466 Å for the S_{-1}, S_0(a), S_0(b), S_1, S_2(R), S_2(C) and S_3 state structures, respectively. For **2**, the Ca-coordinated AcOH9 and AcOH10 were shifted. This indicates that the t-butyl groups are important to cover the Mn_4CaO_4 core from the solvent. Therefore, the inclusion of the t-butyl groups in the theoretical model is required to clearly identify the state that the X-ray structure represents. For the Mn_4CaO_4 and Mn_4Ca moieties, the RMSD values are in the following order: S_0(b) < S_1 < S_0(a) < S_{-1} < S_2(C) < S_2(R) < S_3(C). These results show that the deformations of the Mn_4CaO_4 cores are larger in the S_2 and S_3

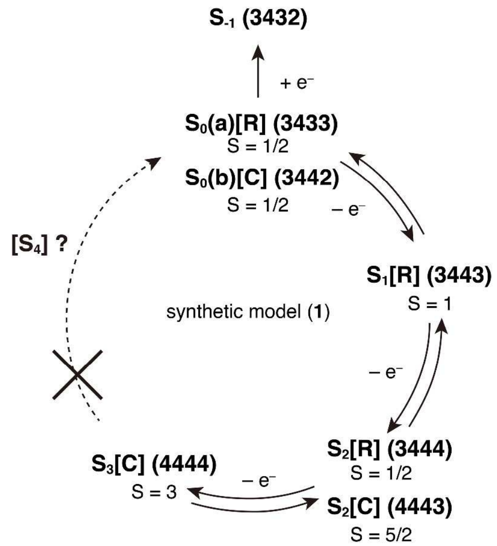

Fig. 2 Illustration of the valence state changes of **1** in the S_i (*i* = –1 - 3) oxidation states revealed by the present DFT calculations. Formal Mn valence states are shown in parentheses in the order of Mn1, Mn2, Mn3 and Mn4.

states. These results can be explained by the fact that structural changes from S_1 to S_0(b) are mainly observed for the elongations of the Mn4-O:TBAA bonds, and these do not significantly contribute to the deformation of the Mn_4CaO_4 core. On the other hand, for the S_2 and S_3 states, the Mn*X*-O5 bonds (*X*=1,4) are largely changed upon oxidation, which contributed to distorting the Mn_4CaO_4 cores.

It is also shown that the RMSD values for the Mn_4Ca and Mn_4CaO_4 cores are similar to the values calculated using the reduced model (**2**). Therefore, the t-butyl groups do not significantly deform the Mn_4Ca core structure. In the next section, more detailed structural changes around the Mn sites are discussed from the viewpoint of their Jahn-Teller distortions[29,37].

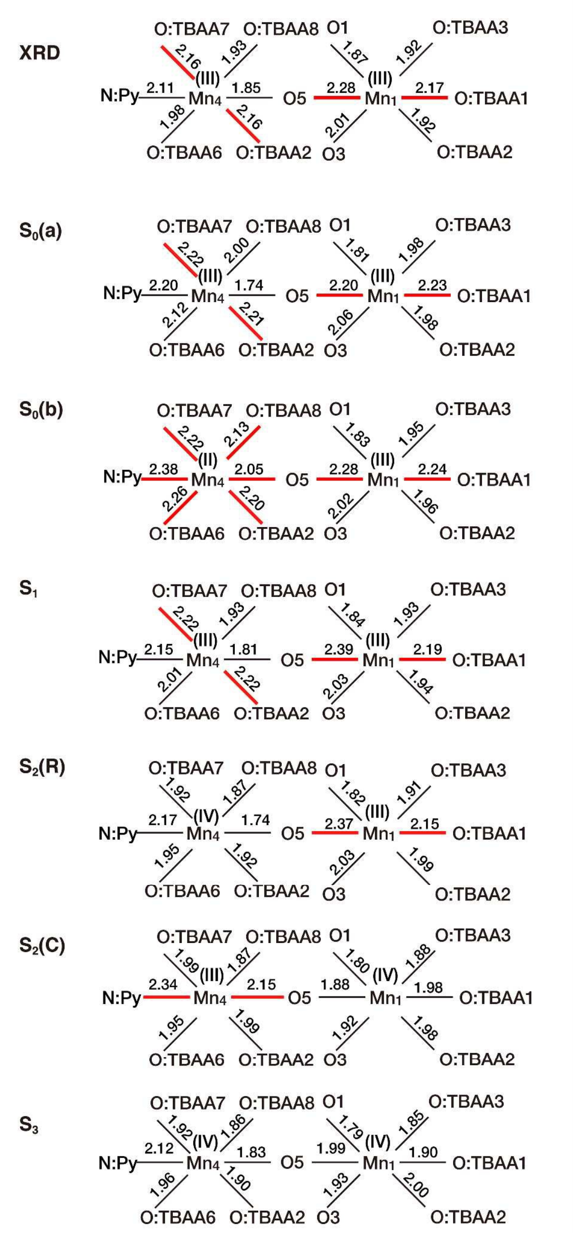

Fig. 3 Comparisons of the coordination bond lengths around Mn1 and Mn4. The Jahn-Teller axes of Mn(III) atoms are shown as red lines.

3.2 Mn Jahn-Teller (JT) distortions

The Mn(III) ion is characterized by its unique Jahn-Teller (JT) distortion. Because the Mn(III) atom possesses four singly occupied d orbitals; three t_{2g} and one e_g orbitals, and the e_g orbital interacts antibondingly with the coordinating ligand orbitals, the Mn-coordination lengths are strongly elongated in the same directions as the e_g orbital distribution.[37-39] In accordance with this, the optimized bond lengths around the Mn ions exhibited the JT distortions in **1**. In Figure 3, the JT principle axes for Mn4 and Mn1 are indicated by the bold red lines, together with the coordination distances. The d orbitals responsible for the JT effect are clearly depicted by the localized natural orbitals (LNOs)[27]. The LNOs are constructed by orbital localization for the singly occupied natural orbitals in the highest spin state. These LNOs are mainly localizing on one spin site (in the present study, the d orbitals on each Mn atom), and the LNOs are very useful for identifying the electronic structure. As an example, the LNOs of the e_g (non t_{2g}) type orbitals for the Mn(III) sites in the S_1 and S_2 states are shown in Figure 4, and all of the LNOs are shown in the supporting material (Figure S2.2-S2.7).

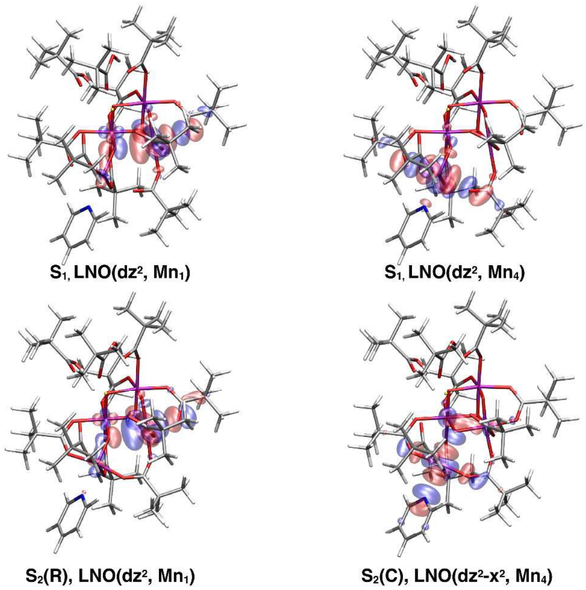
S_1, LNO(dz^2, Mn_1) S_1, LNO(dz^2, Mn_4)

S_2(R), LNO(dz^2, Mn_1) S_2(C), LNO(dz^2-x^2, Mn_4)

Fig. 4 Localized natural orbitals (LNOs) mainly contribute to the Mn Jahn-Teller distortions. The direction of similar LNOs of Mn_1 in the S_1 and S_2(R) states is responsible for the elongations of the Mn_1-O5 and Mn_1-O:TBAA1 bonds in the S_1 and S_2(R) (and also XRD, S_0(a) and S_0(b)) structures in Fig. 3. The direction of LNO of Mn_4 in the S_1 state is responsible for the elongations of the Mn_4-O:TBAA7 and Mn_4-O:TBAA2 bonds in the S_1 (and also XRD, S_0(a) and S_0(b)) structures. The direction of LNO of Mn_4 in the S_2(C) state is responsible for the elongations of the Mn_4-O5 and Mn_4-N:Py bonds in the S_1 (and also S_0(b)) structures. All the Mn LNOs are shown in the supporting material (Figures S2.2-S2.7).

Table 2. Calculated effective exchange integrals (J /cm^{-1} values) of **1** at the UB3LYP/DZVP level.[a]

State	S_0(a)	S_0(b)	S_1	S_2(R)	S_2(C)	S_3
$J_{1,2}$	-38.07	-40.08	–30.19	–21.67	39.57	33.75
$J_{1,3}$	4.52	11.76	15.76	9.32	–12.23	–16.24
$J_{1,4}$	-22.16	-7.52	-5.45	–20.48	–12.85	–11.52
$J_{2,3}$	-53.18	21.16	18.49	15.54	27.81	25.39
$J_{2,4}$	3.36	-1.76	0.22	1.63	–1.01	1.57
$J_{3,4}$	-30.04	-36.48	–0.39	–16.63	–17.62	–5.23

[a] Full geometrical optimizations were also performed at the same UB3LYP/DZVP level.

As clearly shown in Figure 4, the e_g orbitals for Mn1(III) are always the d_{z2} type with the O5-Mn1-O:TBAA1 JT principle axis (z axis) in accord with the JT distortion in the S_0(a), S_0(b) and S_2(R) structures of Figure 3. On the other hand, for the Mn4(III) orbitals, they have a major d_{z2} component with the O:TBAA7-Mn4-O:TBAA2 JT principle axis, though in the S_2(C) state, the LNO for Mn4(III) has a substantial component for the N:Py-Mn4-O5 direction. The difference in the Mn4 LNOs can be attributed to the geometric restriction of **1**, because in the S_2(C) state, Mn4 and Mn1 are directly bridged by μ-O5, thus shortening Mn1(IV)-O5, and in turn, elongating the Mn4(III)-O5 distance. The weak coordination of the N-site of Py to Mn4(III) also contributes to the JT elongation of the N:Py-Mn4-O5 axis.

In the S_0(b) state, there are two e_g type LNOs for Mn4(II) and one for Mn1(III). In the S_0(a) state, one e_g type LNO was found for each of the Mn4(III), Mn3(III) and Mn1(III). The e_g orbitals for Mn4 and Mn1 in S_0(a) are very similar in shape to those in the S_1 state. The e_g orbital for Mn3 in S_0(a) is the pure d_{z2} type with the O5-Mn3-O:TBAA4 JT principle axis. Therefore, the main JT principle axes for the Mn4, Mn3 and Mn1 sites are O: TBAA7-Mn4-O: TBAA2, O5-Mn3-O: TBAA4, and O5-Mn1-O: TBAA1, respectively, as illustrated in Figure 3, though only the JT distortion on Mn4(III) in the S_2(C) state contains some N:Py-Mn4-O5 components.

In the two-electron oxidation (S_3) state, four Mn sites are all in the Mn(IV) valence configuration, thus no JT effect is observed around the Mn-ligand lengths. For example, the Mn1-O5 bond length was reduced by ~0.4 Å upon the one-electron oxidation of the Mn1(III) ion in the S_2(R) to the S_3 state. The optimized Mn_3CaO_4 cubane moiety of S_3 is compatible with the Christou model complex [Ca-Mn(IV)$_3$CaO$_4$][13].

In the native OEC structure of the S_1 state revealed by XRD[2] and XFEL[3], the Mn4 e_g orbital is considered to be the d_{z2} type, in which the z axis is directed to the Mn4-O5-Mn1 as illustrated in Figure S1.1. This result in the JT axis is different from that of **1**, which can be attributed to the geometric restriction of the Mn_4CaO_4 core in **1**, where Mn1 and Mn4 are directly bonded by μ-O5 and a carboxyl ligand (TBAA2). Therefore, elongations of both the Mn4-O5 and Mn1-O5 are impossible for **1**. During the one-electron oxidation (S_2 state) of the native OEC, either Mn4 or Mn1 becomes a Mn(III) state as in the case of **1**, and each Mn(III) site has the similar elongation axis in the O5 direction as that observed in **1**. In fact, in the native OEC S_2(R) state, the Mn4(IV)-O5 bond length becomes shorter to 1.8~1.9 Å by the loss of the JT distortion, and the O5-Mn1(III) bond length becomes longer to 3.0~3.2 Å. On the other hand, in the S_2(L) state, the reverse tendency was predicted on theoretical grounds[33,34]. As the Mn valence state changes between Mn1 and Mn4, the O5 shift is clearly observed in the native OEC with the change in the bond length.

3.3 Spin states

Two EPR signals were observed for the one-electron oxidation state of **1**[15], indicating that two different spin states (S = 1/2 and 5/2) exist similar to the S_2 state of the native OEC. In order to determine the spin states for the ground and low-lying excitation states, all the magnetic interactions among the Mn spin sites were evaluated. Six effective exchange integrals (the inter-site J_{ab} values defined by the $H = -2\Sigma J_{ab}S_aS_b$ Heisenberg spin Hamiltonian) were calculated from eight broken-symmetry solutions using the generalized spin projection methodology[28]. We have demonstrated that the UB3LYP/DZVP method properly reproduced the J values for various transition metal complexes.[23-25] The calculated J values by UB3LYP/DZVP are summarized in Table 2. By solving the spin Hamiltonian, all the pure quantum spin states are obtained (the spin states and excited energies are summarized in Table 3). In Figure 5, all the magnetic interactions are graphically illustrated. By tracing the strong magnetic interactions (connected by bold lines in Figure 5), the stable spin alignment can be easily reproduced. Their local spin correlation factors evaluated for the S_i states (i = 0-3) by solving the spin Hamiltonian are summarized in the supporting material.

In the S_0 state, both the S_0(a) and S_0(b) structures take the S=1/2 ground spin states. In the S_0(a) state, strong antiferromagnetic interactions were observed for $J_{1,2}$, $J_{2,3}$, $J_{3,4}$ and $J_{4,1}$, and the ground state is S=1/2 with an alternating spin polarization (↑↓↑↓). This state is similar to the lowest Sz=1/2 (↑↓↑↓) BS solution.

In the S_0(b) state, the strong antiferromagnetic interactions were calculated for $J_{1,2}$ and $J_{3,4}$. Compared to S_0(a), the $J_{2,3}$ interaction becomes more ferromagnetic. However, the ground spin state still takes an alternated spin polarization (↓↑↓↑) with S=1/2.

Table 3. Low-lying excitation states (ΔE /cm^{-1}) of **1** by solving the Heisenberg spin Hamiltonian ($H = -2JSS$) with the calculated J values at the UB3LYP/DZVP level.

States	S_0(a)	S_0(b)	S_1	S_2(R)	S_2(C)	S_3
0	S = 1/2	S = 1/2	S = 1	S = 1/2	S = 5/2	S = 3
1	S = 3/2	S = 1/2	S = 0,	S = 3/2,	S = 7/2,	S = 2,
	ΔE =92.1	ΔE =58.7	ΔE =0.51	ΔE =2.86	ΔE =69.4	ΔE =16.5
2	S = 5/2	S = 3/2	S = 2,	S = 5/2,	S = 3/2,	S = 4,
	ΔE =247.2	ΔE =61.1	ΔE =1.85	ΔE =38.6	ΔE =91.3	ΔE =36.7
3	S = 1/2	S = 3/2	S = 3,	S = 3/2,	S = 5/2,	S = 3,
	ΔE =310.6	ΔE =104.7	ΔE =9.63	ΔE =106.7	ΔE =132.2	ΔE =40.0

In the S_1 state, the calculated $J_{1,3}$, $J_{2,3}$ were strongly ferromagnetic, while the calculated $J_{1,2}$ was strongly antiferromagnetic. Though the calculated lowest BS configuration was (↑↓↑↓) with Sz=0, the (↓↑↑↑) BS configuration with Sz=3 was calculated to be very low (the energy difference is 32 cm^{-1}). As a very narrow energy gap was observed in the BS configurations, the exact diagonalization of the spin Hamiltonian matrix was required to elucidate the energy levels of the ground and lower-lying excited states. The spin states for the ground, first, second and third- excited states are S=1, S=0, S=2 and S=3, and their excitation energies are only 0.51, 1.85 and 9.63 cm^{-1}, respectively. This result indicates that there exist many low-lying excited states in the S_1 state. The ground spin state with S=1 obtained by the exact diagonalization takes a (↓↑↑↑) spin polarization in contradiction to the lowest BS configuration (↑↓↑↓) with Sz=0. The experimentally observed broad parallel-mode electron paramagnetic resonance (EPR) signal at g=12 is attributed to the signals from the ground triplet state. In the case of the native OEC, the triplet is in the first excited state after the refinement of the BS result by the exact diagonalization[40] and a temperature-dependent parallel mode EPR signal can be observed[41].

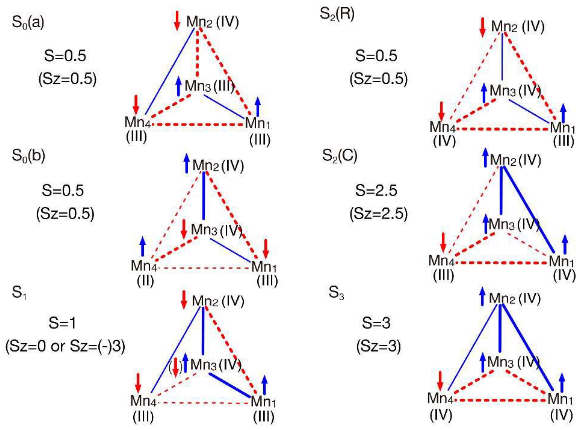

Fig. 5 Schematic illustrations of the magnetic interactions for the Mn spin sites of **1** in the S_0, S_1, S_2 and S_3 states. Red dashed lines and blue solid lines represent the antiferromagnetic and ferromagnetic interactions, respectively. Bold and thin lines represent strong and weak magnetic interactions, respectively. All the values of the magnetic interactions are summarized in Table 2. S (Sz) values indicate the ground quantum (classical/BS) spin states.

In the S_2 state, different ground spin states are calculated for the different S_2 structures. In the S_2(R) state, relatively strong antiferromagnetic interactions were obtained for $J_{1,2}$, $J_{1,4}$ and $J_{3,4}$. The ground spin state becomes S = 1/2, and the first excited state after the exact diagonalization is S = 3/2 with a very low excitation energy (ΔE = 2.86 cm^{-1}). In the S_2(C) state, the calculated $J_{1,2}$ and $J_{2,3}$ were strongly ferromagnetic interactions and the $J_{1,4}$ and $J_{3,4}$ were strong antiferromagnetic interactions. The ground spin state becomes S = 5/2, and the first excited state by the exact diagonalization is S = 7/2 with a higher excitation energy (ΔE = 69.4 cm^{-1}). Based on the calculated local spin correlation factors, the ground spin structures of S_2(R) and S_2(C) can be described as (↑↓↑↓) of Sz =1/2 and (↑↑↑↓) of Sz =5/2, respectively, supporting the BS spin structures for the S_2 state. The ground spin states of S = 1/2 in S2(R) and S = 5/2 in S_2(C) correspond to the two experimentally different S_2-state signals at g = 2.0 and g = 4.9, respectively, determined by EPR spectroscopy. The ground S = 5/2 state of S_2(C) is lower in energy than the ground S = 1/2 of S_2(R) by 0.67 kcal mol^{-1}. For the native OEC, S_2(R) is more stable than the S_2(L) by 2-12 kcal mol^{-1}. [33, 34] The ground spin states of the native OEC are also S = 1/2 and S = 5/2 in S_2(R) and S_2(L), respectively, and their spin structures are (↑↓↓↑) and (↑↑↑↓), respectively[33,34,42,43]. Therefore, the synthetic complex and native OEC take the same ground spin states. However, their spin structures are different, which can be explained by the fact that **1** possesses a substantial antiferromagnetic $J_{1,4}$ interaction, which is in apparent contrast to the negligibly small $J_{1,4}$ interaction in the native OEC. Therefore, the computational results for **1** were totally compatible with the observed EPR results by Zhang et al.[15], and there exist some small differences in the spin structures between **1** and the native OEC.

In the S_3 state, the ground spin state is S = 3 with the (↑↑↑↓) spin polarization. This ground state is similar to the (↑↑↑↓) spin alignment in the S_z=3 BS configuration. It is noteworthy that the ground spin structure of S_3 is very similar to that of S_2(C). The same situation was obtained for the S_3 state of OEC of PSII[44]. The highest-spin ground configuration of the Mn(IV)$_3$CaO$_4$ core of **1** was also consistent with the HS (S = 9/2) ground state observed for the [CaMn(IV)$_3$CaO$_4$] complex[13].

3.4 Theoretical modeling of the synthetic model

As discussed above, the S_1 state of the theoretical model (**1**) well reproduced the characteristic geometric and electronic structural features of the native OEC; however, in contrast to the native OEC, a substantial magnetic interaction between Mn1 and Mn4 exists in **1**. In the native OEC, the distance between Mn1 and Mn4 is *R* ~ 5.0 Å, and the corresponding distance in **1** is *R* = 3.6 Å. Therefore, the shorter distance between Mn1 and Mn4 with the μ-O5 bridge and the carboxyl ligand (TBAA2) in **1** is may be one of the reasons responsible for the difference in the magnetic interaction. Another difference in the native OEC is that the O4 atom is missing in **1**. In order to more closely mimic the native Mn_4CaO_5 core, the incorporation of O4 and elongation of the Mn1-Mn4 distance are the next challenging issues for the synthetic models. In this section, theoretical modelings were carried out by substituting the ligands with other proper ligands in order to predict model complexes more closely resembling the native Mn_4CaO_5 core structure. For the theoretical calculations, a reduced model **2** was used to minimize the computational costs. As discussed in the previous section 3.1, the substitution of tert-butyl to a methyl did not significantly change the Mn_4CaO_4 core structure. For more detailed results of **2**, see the supporting material and reference 45.

(A) Model **A**; AcO2 substituted by two water molecules

The AcO2 is a major candidate to shorten the Mn1-Mn4 length in **2** (**1**) as can be seen in Figure 1. The AcO2 ligand in **2** is substituted with two water molecules (Wat1 and Wat2) in a putative model referred to as model **A**. Model **A** was fully optimized to determine if the Mn1-Mn4 distance had changed. It was found that almost no structural changes were observed for the Mn_4CaO_4 core, and the Mn1-Mn4 length is unchanged (from *R*(Mn1-Mn4) = 3.63 Å to *R*(Mn1-Mn4) = 3.64 Å) by simply removing the connecting ligand (AcO2) of **2**.

(B) Model **B**; AcO7 additionally substituted by μ-O4

In addition to the substitution made in model A, another putative model **B** was constructed by substituting the carboxyl ligand (AcO7) bridging between Mn3 and Mn4 with a μ-O4 atom. By using this model **B**, the Mn1-Mn4 length increased to *R*(Mn1-Mn4) = 4.3 Å, the Mn1-O5 length becomes longer than the Mn4-O5 length (*R*(Mn1-O5) = 2.41Å and *R*(O5-Mn4) = 1.88Å), and the Mn4 moved into the Mn1-O3-Mn3-O5- plane. The Mn_4CaO_5 core of model **B** became topologically very similar to the native OEC core in the S_1 state, however, the Mn1-Mn4 length is still shorter by 0.7 Å compared to the native OEC.

(C) Models **Ca** and **Cb**; AcOH9 and AcOH10 additionally substituted by two water molecules (Wat3 and Wat4)

By comparison with the native OEC, model **B** is still different regarding the coordination environment around the Ca^{2+} ion. In the native OEC, two water molecules (W3 and W4) are coordinated to the Ca^{2+} ion in the region closer to the Mn1 side from the Mn2-Ca-O5-O3 plane. On the other hand, for models **A** and **B**, one of the Ca-coordinating ligands (AcOH9) is located on the opposite side (Mn3 side). In order to investigate the effects of the Ca ligand coordination, the bulky Ca^{2+} coordinating ligands (AcOH9 and AcOH10) are substituted by water molecules in addition to the modifications introduced in model **B**. The resulting models are

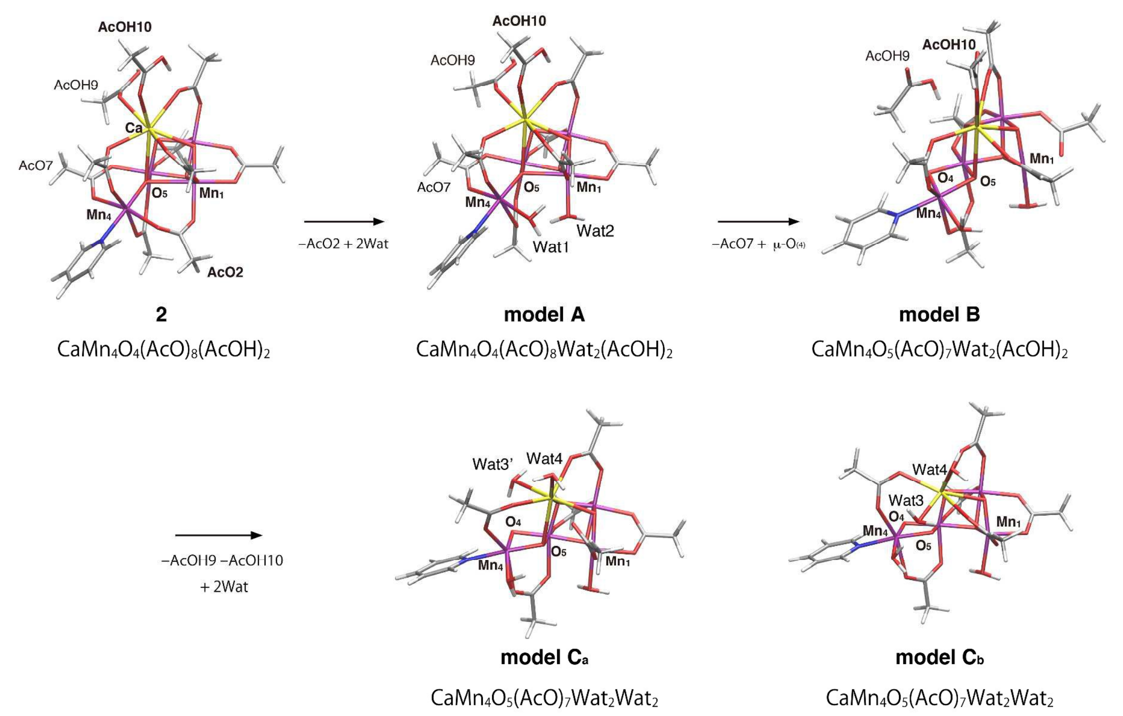

2
$CaMn_4O_4(AcO)_8(AcOH)_2$

model A
$CaMn_4O_4(AcO)_8Wat_2(AcOH)_2$

model B
$CaMn_4O_5(AcO)_7Wat_2(AcOH)_2$

model Ca
$CaMn_4O_5(AcO)_7Wat_2Wat_2$

model Cb
$CaMn_4O_5(AcO)_7Wat_2Wat_2$

Fig. 6 Theoretical modeling of the S_1 state by substituting the ligands of **2** in order to model the Mn_4CaO_5 core of the native OEC more closely. **2** is a reduction model of **1** by modelling the pivalic acids (Bu^tCOO) to acetic acids(AcO).The full molecular structures after full geometrical optimizations are shown. The optimizations were performed at the UB3LYP/DZVP level in the highest spin state.

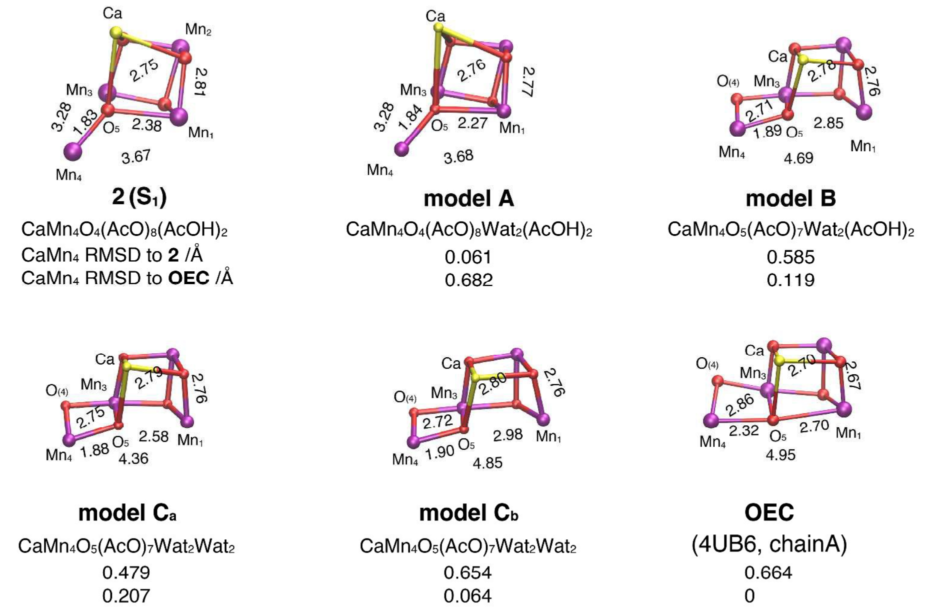

Fig. 7 The Mn_4CaO_X cores of the theoretical models (**2**, **A**, **B**, **Ca** and **Cb**) with key distances depicted in the Å (*R*(Mn4-O5), *R*(O5-Mn1), *R*(Mn4-Mn3), *R*(Mn3-Mn2), *R*(Mn2-Mn1), *R*(Mn1-Mn4)). For the full molecular structures, see Figure 5.

designated models **Ca** and **Cb**, in which model **Ca** has two water molecules in the original Ca-coordinating ligand orientations (Wat3' and Wat4) and model **Cb** has a Ca^{2+}-coordinating ligand orientation similar to the native OEC (Wat3 and Wat4). The stabilities of **Ca** and **Cb** are almost the same (**Cb** is slightly more stable than **Ca** by 0.08 kcal mol^{-1}), however, the Mn1-Mn4 lengths are *R*(Mn1-Mn4) = 4.4 Å and *R*(Mn1-Mn4) = 4.8 Å for **Ca** and **Cb**, respectively. In **Cb**, the carboxyl ligand bridging Ca and Mn4 (AcO8) shifted to the O4 side, and its carboxyl group is located on the Ca-O5-Mn4 plane. Therefore, the ligand coordination of the AcOH9 position tends to slide the AcO8 to the AcO3 side by steric repulsions. These results suggest that the position of W3 is important for increasing the Mn1-Mn4 distance, and this elongation may be important for the formation of the labile Mn1-O-Mn4 bond that is responsible for promotion of the molecular oxygen formation reaction in the native OEC[29,33].

In Figure 6, full molecular structures for the theoretical model calculations are shown. In Figure 7, only the Mn_4CaO_x ($_x$ =4, 5) cores are shown with the key Mn-O and Mn-Mn distances. The RMSD values compared to the synthetic model (**2** in the HS S_1 state) and the native OEC are also shown in Figure 7. The RMSD values for the native OEC are 0.664, 0.682, 0.119, 0.207, and 0.064 Å for **2**, models **A**, **B**, **Ca**, and **Cb**, respectively. These values quantitatively demonstrate that model **A** is close to **2** (**1**), model **B** becomes much closer to the native OEC, but still not a best match, model **Ca** does not improve the structural similarity, and model **Cb** most closely resembles the native Mn_4CaO_5 core structure.

Based on these computational results, removal of the AcO2 and AcO7 anions in **2**(**1**) and the O4 addition to the Mn_4CaO_4 core were crucially important in order to improve the native OEC structural features. The substitution of AcOH9 and AcO10 on the Ca^{2+} ion with two water molecules followed by their appropriate conformational changes may have a deep influence on the highly sophisticated catalytic mechanism of the native OEC. This may be closely related to the particular important role of Ca^{2+} ion during the OEC catalytic cycle.[30] On the other hand, the pyridine molecule (Py) coordinated to the Mn4 ion has little influence on the Mn_4CaO_4 core, and the Py is replaced by a water molecule. The site can also be replaced by ammonia in the ammonia-treated OEC[46]. On the other hand, the water molecule coordinated to the Mn1 ion was occupied by a histidine (His332) side chain in the native OEC. This indicates that His332 does not play a significant role in the determination of the geometric structure of the Mn_4CaO_5.

3.5 Theoretical substitutions of Ca^{2+} ion with divalent ions

The present DFT calculations revealed crucial roles of the Ca^{2+} ion in the OEC. Substitution of the Ca^{2+} ion with the Sr^{2+} ion was feasible in the native OEC, preserving the ability of water oxidation of the Mn_4SrO_5 cluster[47]. Theoretical substitutions of the Ca^{2+} ion with several divalent ions are interesting due to lacking such experimental results for **1**. The full geometry optimizations of the putative clusters obtained by substitutions of the Ca^{2+} ion with divalent ions A^{2+} (=Ba^{2+}, Sr^{2+}, Mn^{2+}, Zn^{2+} and Mg^{2+}) in **2** were performed to elucidate variations in the Mn-Mn, Mn-O and A^{2+}-O distances. Their optimized distances in the S_1 state of **2** are summarized in the supporting material (Tables S6.1 and S6.2). The optimized Mn1-Mn2 distances were about 2.8 Å, indicating no significant difference among the Mn_4O_4 clusters with the different divalent ions. The Mn1-Mn3, Mn1-Mn4, Mn2-Mn3 and Mn3-Mn4 distances were 3.1~3.2, 3.6~3.7, 2.7 and 3.2 (Å), respectively, similarly showing no variations in each distance. The Mn-Mn skeletons of **2** were robust for substitutions of the Ca^{2+} ion by them, indicating the possible synthesis of such derivatives of **2** as in the native OEC. The Mn-Mn distances of about 2.7 and 2.8 (Å) in the derivatives are also comparable to the XFEL and EXAFS results for the native OEC.

The A^{2+}-O5 distances were 2.9~3.0 (Å), indicating small variations by substitutions of the divalent ions. On the other hand, the A^{2+}-O1 and A^{2+}-O2 distances were variable, depending on the types of the divalent ions. The averages of these distances were 2.77(1.35), 2.62(1.18), 2.52(1.12), 2.27(0.83), 2.23(0.74) and 2.22(0.72) (Å), respectively, for Ba^{2+}, Sr^{2+}, Ca^{2+}, Mn^{2+}, Zn^{2+} and Mg^{2+}, with the corresponding ionic radii[48,49] given in parentheses. The average A^{2+}-O^{2-} distances decreased with a decrease of the ionic radii, indicating an increase in the binding energies. The average Ca-O distance (2.52 Å) in **1** was similar to the Ca-O distance between Ca and the coordinated water molecule in OEC. This implies that the water exchange was too fast for the Ba^{2+} derivative due to the very weak Ba^{2+}-H_2O coordination energy. On the other hand, the water exchange was too slow for the Zn^{2+} and Mg^{2+} derivatives due to the too strong coordination, indicating that the intermediate characteristics of Sr^{2+} and Ca^{2+} are favourable for water binding in OEC. Thus selection of the appropriate divalent metal ions is also important for the catch and release of substrate water molecules for the water oxidation during artificial photosynthesis.

4. Conclusions

The geometric and electronic structures of the synthetic model complex **1** were revealed for the four oxidation states, corresponding to the $S_{0\text{-}3}$ states of the native OEC as shown in Figure 2, at the broken-symmetry (BS) density functional theory (DFT) followed by the exact diagonalization of the spin Hamiltonian model using the effective exchange integrals obtained by the total energies of the BS DFT.

In the S_0 state, two valence states of (Mn1(III), Mn2(IV), Mn3(III), Mn4(III)) and (Mn1(III), Mn2(IV), Mn3(IV), Mn4(II)) were obtained for **1**. Both states take the S=1/2 ground state and the former state is slightly lower in energy than the latter by 2.85 kcal mol^{-1}.

In the S_1 state, only one valence state of (Mn1(III), Mn2(IV), Mn3(IV), Mn4(III)) was found by the geometry optimization, and the S_1 state possesses very low-lying excitation states above the S = 1 ground state. The first excitation state was calculated to be S = 0 with an excitation energy of 0.51 cm^{-1}. The optimized geometric structure in the S_1 state was concluded to correspond to the experimentally determined structure of **1**[15] among all of the calculated states (S_{-1}- S_3) based on the RMSD values calculated for all of the heavy atoms and the Mn_4CaO_4 core atoms.

In the S_2 state, two valence states of (Mn1(III), Mn2(IV), Mn3(IV), Mn4(IV)) and (Mn1(IV), Mn2(IV), Mn3(IV), Mn4(III)) were obtained. Their ground spin states are S = 1/2 and S = 5/2, respectively, in accord with the EPR results for **1**[14]. The latter state is slightly more stable than the former by 0.67 kcal mol^{-1}. A very small shift in the position of O5 was found between the two different valence states, which is in sharp contrast to that of the native OEC[29,33,34].

In the S_3 state, a uniform valence state of (Mn1(IV), Mn2(IV), Mn3(IV), Mn4(IV)) resulted, showing an almost symmetrical Mn1-O5-Mn4 bond. The ground spin state obtained by the exact diagonalization of the spin Hamiltonian model was S=3 in accord with the ground S = 3 state of OEC[33,34].

The structural changes in the Mn_4CaO_4 core are very limited for all of the oxidation states, indicating that the synthetic model complex is rather “rigid”. The major reason for this is that the O5 atom is closely bound to both the Mn1 and Mn4 ions due to the short Mn1-Mn4 distance. This limits a large O5 shift upon the Mn1 or Mn4 oxidation during the S_1 to S_2 transition, which is in sharp contrast to the native OEC. Thus the model calculations of **1**(**2**) support a theoretical view, namely, the labile nature of the Mn1-O5-Mn4 bond in the native OEC.[20,21] Based on the magnetic interactions revealed by the present study, a moderate antiferromagnetic interaction exists between Mn1 and Mn4 ($J_{1,4}$) in the S_0(a), S_2(R), S_2(C) and S_3(C) states. Therefore, non-negligible differences exist between the synthetic model **1** and native OEC, in spite of the remarkable similarities in their oxidation state, core geometry and ground spin states.

In order to more closely mimic the native Mn_4CaO_5 core structure and analyze the possible effects of the ligand environment, we sequentially substituted several ligands and examined their effects on the structure of the synthetic complex. Starting from the reduced model **2**, several carboxyl groups were replaced by water molecules or O4. It was found that the short Mn1-Mn4 length was not elongated only by substituting the AcO2 connecting Mn4 and Mn1 with water molecules, but the introduction of O4 and correction of the Ca coordinating ligands (Wat3) elongated the Mn1-Mn4 distance significantly, resulting in a structure comparable to that of the native OEC. Therefore, the introduction of O4 and conformational controls of the Ca^{2+} coordinating ligands will be very important for synthesizing model complexes more closely mimicking the native OEC beyond **1**. Theoretical substitutions of the Ca^{2+} ion with other divalent ions (Ba^{2+}, Sr^{2+}, Ca^{2+}, Mn^{2+}, Zn^{2+} and Mg^{2+}) in **1** also elucidated the important roles of the Ca^{2+} and Sr^{2+} ions for catch and release of the substrate water molecule for water oxidation in the native and artificial OECs.

Acknowledgements

Numerical calculations were carried out under the support of (1)”Interdisciplinary Computational Science Program” at the Center for Computational Sciences, University of Tsukuba; (2) the HA-PACS Project for advanced interdisciplinary computational sciences by exa-scale computing technology; and (3) the Research Center for Computational Science, Okazaki, Japan. This research was supported by a Grant-in-Aid for Specially Promoted Research (No. 24000018) from MEXT, Japan.

Notes and references

1 V. K. Yachandra, K. Sauer and M. P. Klein, *Chem. Rev., 1996,* **96**(7), 2927.

2 Y. Umena, K. Kawakami, J.-R. Shen, and N. Kamiya, *Nature,* 2011, **473**, 55-60.

3 M. Suga, F. Akita, K. Hirata, G. Ueno, H. Murakami, Y. Nakajima, T. Shimizu, K. Yamashita, M. Yamamoto, H. Ago, and J.-R. Shen, *Nature,* 2015*,* **517**, 99-103.

4 V. K. Yachandra, V. J. DeRose, M. J. Latimer, I. Mukerji, K. Sauer, and M. P. Klein, *Science,* 1993, **260**, 675-679.

5 J. Yano, and V. Yachandora, Chem. Rev., 2014, 114, 4175-4205.

6 M. R. A. Blomberg, T. Borowski, F. Himo, R.-Z. Liao and P. E. M. Siegbahn, *Chem. Rev.,* 2014, **114**, 3601-3658.

7 J.-R. Shen, *Annu. Rev. Plant Biol.* 2015, **66**, 23-48.

8 J. Yano, et al. *Proc. Natl. Acad. Sci. U. S. A.* 2005, 102, 12047-12052.

9 M. Askerka, D.J. Vinyard, J. Wang, G. W. Brudvig and V. S. Batista, *Biochemistry,* 2015, **54**, 1713-1716.

10 C. Kupitz, et al. *Nature,* 2014, **513**, 261-265.

11 J. Kern, et al. *Nat. commun.,* 2014, **5**, 4371.

12 J. S. Kanady, E. Y. Tsui, M. W. Day and T. A. Agapie, *Science,* 2011, **333**, 733-736.

13 S. Mukherjee, J. A. Stull, J. Yano, T. C. Stamatatos, K. Pringouri, T. A. Stich, K. A. Abboud, R. D. Britt, V. K. Yachandra and G. Christou, *Proc. Natl. Acad. Sci. U. S. A.,* 2012, **109** (7), 2257-2262.

14 C. Chen, C. Zhang, H. Dong and J. Zhao, *Dalton Trans.*, 2015, **44**, 4431-4435.

15 C. Zhang, C. Chen, H. Dong, J-R. Shen, H. Dau and J. A. Zhao, *Science,* 2015, **348**, 690-693.

16 K. N. Ferreira, T. M. Iverson, K. Maghlaoui, J. Baber and S. Iwata, *Science,* 2004, **303**, 1831-1838.

17 K. Yamaguchi, K. Ohta, S. Yabushita and T. Fueno, *Chem. Phys. Lett.,* 1977, **49**, 555-559.

18 K. Yamaguchi and T. Fueno, *Chem. Phys.,* 1977, **23**, 375-386.

19 K. Yamaguchi, *Chem. Phys. Lett.,* 1979, **66**, 395-399.

20 K. Yamaguchi, *Chem. Phys. Lett.,* 1979, **68**, 477-482.

21 L. Noodleman, *J. Chem. Phys.,* 1981, **74**, 5737-5743.

22 A. Aizman and D.A. Case, *J. Am. Chem. Soc.*, 1982, **104**, 3269-3279.

23 Y. Kitagawa, T. Matsui, N. Yasuda, H. Hatake, Y. Kawakami, S. Yamanaka, M. Nihei, M. Okumura, H. Oshio and K. Yamaguchi, *polyhedron,* 2013, **66**, 97-101.

24 T. Saito, Y. Kataoka, Y. Nakanishi, T. Matsui, Y. Kitagawa, T. Kawakami, M. Okumura and K. Yamaguchi, *Chem. Phys.,* 2010, **368**, 1-6.

25 S. Yamanaka, K. Kanda, T. Saito, Y. Kitagawa, T. Kawakami, M. Ehara, M. Okumura, H. Nakamura and K. Yamaguchi, *Chem. Phys. Lett.,* 2012, **519**, 134-140.

26 M. Valiev, E. J. Bylaska, N. Govind, K. Kowalski, T. P. Straatsma, H. J. J. van Dam, D. Wang, J. Nieplocha, E. Apra, T. L. Windus and W. A. de Jong, *Comput. Phys. Commun.,* 2010, **181**, 1477-1489.

27 M. Shoji, Y. Yoshioka, and K. Yamaguchi, *Chem. Phys. Lett.,* 2014, **608**, 50-54.

28 M. Shoji, K. Koizumi, Y. Kitagawa, T. Kawakami, S. Yamanaka, M. Okumura, and K. Yamaguchi, *Chem. Phys. Lett.,* 2006, **432**, 343-347.

29 M. Shoji, H. Isobe, S. Yamanaka, M. Suga, F. Akita, J.-R. Shen, and K. Yamaguchi, *Chem. Phys. Lett.,* 2015, **627**, 44-52.

30 I. D. Brown and D. Altermatt, *Acta Cryst.*, 1985, **B 41**, 244-247.

31 H. H. Thorp, *Inorg. Chem.,* 1992, **31**, 1585-1588.

32 W. Liu and H. H. Thorp, *Inorg. Chem.,* 1993, **32**, 4102-4105.

33 H. Isobe, M. Shoji, S. Yamanaka, Y. Umena, K. Kawakami, N. Kamiya, J.-R. Shen, and K. Yamaguchi, *Dalton Trans.,* 2012, **41**, 13727-13740.

34 D. A. Pantazis, W. Ames, N. Cox, W. Lubitz and F. Neese, *Angew. Chem. Int. Ed.,* 2012, **51** (39), 9935-9940.

35 M. Shoji, H. Isobe, S. Yamanaka, Y. Umena, K. Kawakami, N. Kamiya, J.-R. Shen, and K. Yamaguchi, *Catal. Sci. Technol.,* 2013, **3**, 1831-1848.

36 M. Shoji, H. Isobe, S. Yamanaka, Y. Umena, K. Kawakami, N. Kamiya, J.-R. Shen, T. Nakajima, and K. Yamaguchi, *Mol. Phys.,* 2015, **113**, 359-384.

37 K. Yamaguchi, S. Yamanaka, H. Isobe, T. Saito, K. Kanda, Y. Umena, K. Kawakami, J.-R. Shen, N. Kamiya, M. Okumra, H. Nakamura, M. Shoji and Y. Yoshioka, *Int. J. Quantum Chem.,* 2013, **113**, 453-473.

38 H.A. Jahn and E. Teller, *Proc. R. Soc. London A,* 1937, **161**, 220-235.

39 H. Koppel, D.R. Yarkony and H. Barentzen (Eds.), Springer Series in Chemical Physics, 2010, **97**, Springer-Verlag.

40 H. Isobe, M. Shoji, S. Yamanaka, H. Mino, Y. Umena, K. Kawakami, N. Kamiya, J.-R. Shen, and K. Yamaguchi, *Phys. Chem. Chem. Phys.*, 2014, **16**, 11911-11923.

41 H. Mino, A. Kawamori, *Biochim. Biophy. Acta,* 2001, **1503**, 112-122.

42 W. Ames, D. A. Pantazis, V. Krewald, N. Cox, J. Messinger, W. Lubitz, F. Neese, *J. Am. Chem. Soc.,* 2011, **133**, 19743-19757.

43 M. Asada, H. Nagashima, F. H. Koura, J.–R. Shen, A. Kawamori and H. Mino, *Biochim. Biophy. Acta,* 2013, **1827**, 438-445.

44 H. Isobe, M. Shoji, J.-R. Shen, K. Yamaguchi, *J. Phys. Chem. B,* 2015, **119**, 13922-13933.

45 M. Shoji, H. Isobe, T. Nakajima, K. Yamaguchi, *Chem. Phys. Lett.*, 2015, **640**, 23-30.

46 P. Navaro, W. Ames, H. Nilsson, T. Lohmiller, D. A. Pantazis, L. Rapatsskiy, N. M. Nowaczyk, F. Neese, A. Boussac, J. Messinger, W. Lubitz, and N. Cox, *Proc. Natl. Acad. Sci. U. S. A.,* 2013, **110**, 15561-15566.

47 F. H. M. Koua, Y. Umena, K. Kawakami and J.-R. Shen, *Proc. Natl. Acad. Sci. U. S. A.,* 2013, **110**(10), 3889-3894.

48 Y. Q. Jia, J. *Solid State Chem.*, 1991, **95**, 184-187.

49 R. D. Shannon, and C. T. Prewitt, *Act. Cryst.*, 1969, **B 25**, 925-946.